

Contents

1 Theory	3
1.1 X-ray Diffraction Principles	3
1.1.1 Scattering at Lattices	3
1.1.2 X-rays	5
1.2 Sesquioxides	5
1.2.1 Chromium Oxide	6
1.2.2 Gallium Oxide	8
1.3 Heteroepitaxy	9
1.3.1 Pseudomorphic Growth	9
1.3.2 Relaxed Growth	11
Dislocations	11
Slip Systems for Sesquioxide Heterostructures	13
2 Experimental Methods	15
2.1 Pulsed Laser Deposition	15
2.1.1 Setup	16
2.1.2 Plasma Dynamics	16
2.1.3 Segmented Target Approach	18
2.2 X-Ray Diffraction Measurement	18
2.2.1 2θ - ω -scans	19
2.2.2 ω -scans	20
2.2.3 φ -scans	20
2.2.4 Reciprocal Space Maps	21
2.2.5 Technical Aspects	23
2.3 Further Methods	24
2.3.1 Thermal Evaporation	24
2.3.2 Resistivity Measurement	25
2.3.3 Thickness Determination	26
2.3.4 Spectral Transmission	27
3 Experiment, Results and Discussion	29
3.1 Preliminary Investigations	30
3.1.1 Experiment	30
3.1.2 Results	30
Oxygen Partial Pressure Variation on <i>m</i> -plane Sapphire	30
Growth Temperature Variation on <i>m</i> -plane Sapphire	32
Influence of Growth Rate on Crystal Structure	35

	Deposition on <i>c</i> -, <i>r</i> -, <i>m</i> - and <i>a</i> -plane Sapphire	37
3.1.3	Conclusion	39
3.2	Doping of Cr ₂ O ₃ Thin Films	40
3.2.1	Experiment	40
3.2.2	Results	41
	Laser Position Variation for Different Targets	41
	Ohmic Contact Optimization	48
3.2.3	Conclusion	48
3.3	Strain Analysis	50
3.3.1	Experiment	50
	Sample Fabrication	50
	Measurements	51
3.3.2	Results	53
	<i>c</i> -plane: Laser Spot Size Variation	55
	<i>c</i> -plane: Pulse Energy Variation	58
	<i>r</i> -plane: Laser Spot Size Variation	60
	<i>r</i> -plane: Pulse Energy Variation	61
	Appendices	63
A	Calculations	65
A.1	<i>m</i> -plane lattice constants	65
A.2	<i>a</i> -plane lattice constants	66
B	Figures	67

Chapter 3

Experiment, Results and Discussion

Contents

3.1	Preliminary Investigations	30
3.1.1	Experiment	30
3.1.2	Results	30
3.1.3	Conclusion	39
3.2	Doping of Cr₂O₃ Thin Films	40
3.2.1	Experiment	40
3.2.2	Results	41
3.2.3	Conclusion	48
3.3	Strain Analysis	50
3.3.1	Experiment	50
3.3.2	Results	53

3.3 Strain Analysis

The structural properties of the thin film, namely its mosaicity and lattice distortion depend crucially on the growth process. It turned out that the absorption of energy at the laser entrance window alters the growth rate and the crystallinity much more dominantly than the growth temperature or the oxygen partial pressure (cf. 3.1). A similar effect was observed when targets were used for fabrication that exhibit a non-planar surface and tracks that were carved during previous ablations (cf. 3.2). Because the structural properties of the thin film also influence its electrical properties (cf. 3.2), the following investigations focus on the origin of the observed variations in strain and ω -FWHM. This is further motivated by the observation that a deliberate and controlled variation of laser spot size on the target surface yields a large reduction of ω -FWHM as well as a reduced shift of the peak position in the 2θ - ω -pattern (Fig. 3.19). This was achieved by varying the lens position (cf. 2.1) such that the laser spot size increases, yielding smaller fluence and larger ablation area on the target surface.

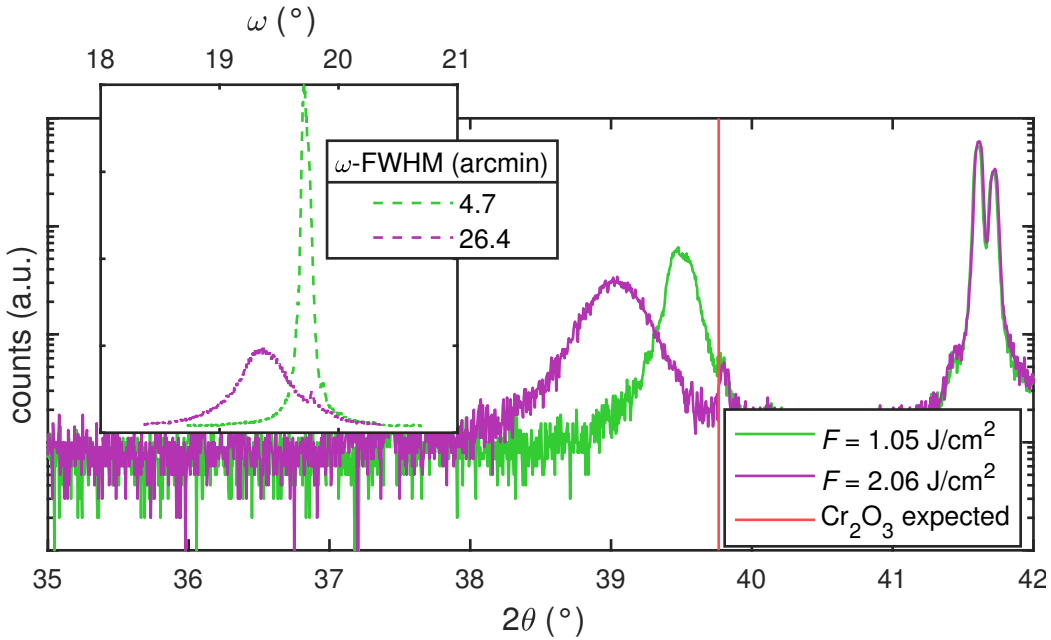


Figure 3.19: 2θ - ω -patterns for two *c*-plane samples fabricated with different laser focus on the target. The inset displays the diffractograms of the corresponding ω -scans performed on the respective reflections. The ZnO-doped (low) target was used without a fixed *rPLD* but with uniform ablation on the whole target surface.

3.3.1 Experiment

Sample Fabrication

For all following depositions, the laser entrance window was cleaned before each process. A pure Cr_2O_3 target was used for deposition of thin films on $5 \times 5 \text{ mm}^2$ sapphire substrates in the four aforementioned orientations. The first batch of samples was produced by only varying the pulse number to achieve a series of thin films with varying

thickness but constant laser fluence during deposition⁽⁹⁾. The pulse energy was set to 650 mJ and the lens position⁽¹⁰⁾ to -2 cm , the resulting fluence is approx. 2 J cm^{-2} . This corresponds to the standard configuration during all previous processes (pink square in Fig. 2.2). This was repeated with fewer pulse number variations for three other lens positions, namely 0 cm , 1 cm and 2 cm , resulting in lower fluences: In Fig. 2.2, the yellow circles represent the probed laser fluences. This set of samples is referred to as the 1st batch.

To investigate the influence of fluence independent of ablation area, a 2nd batch of samples was fabricated with a fixed lens position (-1 cm) but varying laser pulse energy: 300 mJ, 450 mJ, 650 mJ and 800 mJ. The pulse number was adjusted to achieve approximately same thicknesses. The achieved fluences are visualized as red triangles in Fig. 2.2.

Measurements

For all samples, $2\theta\text{-}\omega$ -scans as well as ω -scans were performed. The reflections probed by the latter were (00.6) , (02.4) , (30.0) and (22.0) for *c*-, *r*-, *m*- and *a*-plane, respectively. For some selected samples of different thickness and fluence from the 1st batch, transmission measurements have been performed. The thickness of all samples was determined by spectroscopic ellipsometry measurements. To obtain more information about the relation between in-plane and out-of-plane lattice constants, Reciprocal Space Maps (RSMs) were performed on selected samples:

c-plane For *c*-plane samples, the thickness series of the 1st batch that was fabricated with the largest laser spot size (lowest fluence) was investigated. The asymmetric reflection that was used for probing the relaxation process is (02.10) , which has an inclination angle of approx. 32° with respect to the sample surface.

r-plane All *r*-plane samples fabricated in the 2nd batch with different laser pulse energies were investigated. For each sample, the *x*-axis of the sample – containing the projection of the *c*-axis – is found by performing a φ -scan on the (03.0) reflection: This set of lattice planes has an inclination with respect to the surface, so the position of the peak in the diffraction pattern of the φ -scan reveals the *x*-axis. In this azimuth, an RSM is recorded around the asymmetric (03.0) reflection and the symmetric (02.4) reflection. By rotating $\Delta\phi = 90^\circ$, the *y*-axis lays in the scattering plane and another RSM is performed around the symmetric (02.4) reflection. The twofold measurement of the symmetric reflection is necessary to calculate a possible lattice plane tilt for both *x*- and *y*-direction. Note that no shear is calculated due to the asymmetric nature of the (03.0) reflection with respect to the *r*-orientation⁽¹¹⁾. After performing the various

⁽⁹⁾ The series of thicknesses that was achieved in the prior experiments was correlated to a series of growth rates.

⁽¹⁰⁾ Note that the values for the lens position have an arbitrary offset; a value of 0 cm does not correspond to the position where the target surface is in focus.

⁽¹¹⁾ For *m*- and *a*-plane rhombohedral structures, the crystal is symmetric under the transformation $\phi \rightarrow \phi + 180^\circ$, which is not the case for *r*-plane.

corrections described in 2.2.4, the tilt angles can be calculated for both azimuths by

$$\theta = \arccos \left(\frac{q_{\perp}}{|\mathbf{q}|} \right) \cdot \text{sgn}(q_{\parallel}) , \quad (3.4)$$

with q_{\perp} and q_{\parallel} being the out-of-plane (o.o.p.) and in-plane (i.p.) components of the scattering vector \mathbf{q} , respectively. The i.p. and o.o.p. strains are determined by comparing the observed scattering vector to the expected scattering vector for the (03.0) reflection:

$$\mathbf{q}_{(03.0)} = |\mathbf{q}_{(03.0)}| \cdot \begin{pmatrix} \cos \alpha_{(03.0)|r} \\ \sin \alpha_{(03.0)|r} \end{pmatrix} , \quad (3.5)$$

with $|\mathbf{q}_{(03.0)}|$ calculated from Equ. (2.6) and Equ. (2.7). $\alpha_{(03.0)|r}$ denotes the angle between the (03.0) reflection and the normal of the r -planes; it can be calculated from Equ. (2.8):

$$\alpha_{(03.0)|r} = 90^\circ - (\alpha_{(03.0)|c} - \alpha_{(01.2)|c}) = \alpha_{(01.2)|c} = 57.62^\circ . \quad (3.6)$$

***m*-plane** Similar to above, all *m*-plane samples from the 2nd batch were investigated. The samples were aligned to the x -axis by performing a φ -scan on the asymmetric (30.6) reflection, and an RSM was recorded afterwards. By rotating $\Delta\phi = 180^\circ$ while maintaining 2θ and ω , the scattering condition for (30. $\bar{6}$) is probed and an RSM was recorded. The symmetric reflection (30.0) was also measured in this azimuth. The tilt angle and shear angle can be calculated according to Equ. (3.4) and Equ. (2.13), respectively. The lattice constants can be calculated from the components of the scattering vectors:

$$a_{\perp} = \frac{\sqrt{12}}{q_{\perp}^{(30.\pm 6)}} , \quad (3.7)$$

$$a_{\perp} = \frac{\sqrt{12}}{q_{\perp}^{(03.0)}} , \quad (3.8)$$

$$c = \frac{6}{q_{\parallel}^{(30.\pm 6)}} . \quad (3.9)$$

a_{\perp} denotes the a lattice constant in direction of the normal to the sample surface. By rotating $\Delta\phi = 90^\circ$, the y -axis can be probed via asymmetric reflections (42.0) and (22.0), which differ in the azimuth by $\Delta\phi = 180^\circ$. A second symmetric reflection (30.0) is recorded in this azimuth. Similar to the x -axis, the tilt and shear angles, as well as the lattice constants can be calculated:

$$(4\bar{2}.0) : a_{\perp} = \frac{\sqrt{12}}{q_{\perp}^{(4\bar{2}.0)}} , \quad a_{\parallel} = \frac{2}{q_{\parallel}^{(4\bar{2}.0)}} , \quad (3.10)$$

$$(22.0) : a_{\perp} = \frac{\sqrt{12}}{q_{\perp}^{(22.0)}} , \quad a_{\parallel} = \frac{2}{q_{\parallel}^{(22.0)}} , \quad (3.11)$$

$$(30.0) : a_{\perp} = \frac{\sqrt{12}}{q_{\perp}^{(03.0)}} . \quad (3.12)$$

a_{\parallel} denotes the a lattice constant parallel to the y -axis. For detailed calculations of the former equations, see A.1. Note that all 6 measured reflections yield a value for a_{\perp} ,

and 2 measured reflections each yield 2 values for c and a_{\parallel} , respectively. Therefore, for each lattice constant, the mean value is evaluated and the error is estimated by the standard deviation.

***a*-plane** All a -plane samples from the 2nd batch were investigated and the method is similar to the one applied to the m -plane samples. The azimuth of the x -axis is found by performing a φ -scan on the (22.6) reflection, which also served for an RSM. Rotating by $\Delta\phi = 180^\circ$ yields the (22.6̄) reflection and (22.0) is also measured. Similar to above, the sample is rotated by 90° to align to the y -axis and two more asymmetric reflections are recorded: (30.0) and (03.0). A second RSM of (22.0) is also performed. This yields the following lattice constants for the x -axis:

$$a_{\perp} = \frac{4}{q_{\perp}^{(22.\pm 6)}}, \quad (3.13)$$

$$a_{\perp} = \frac{4}{q_{\perp}^{(22.0)}}, \quad (3.14)$$

$$c = \frac{6}{q_{\parallel}^{(22.\pm 6)}}, \quad (3.15)$$

and for the y -axis:

$$(30.0) : a_{\perp} = \frac{2}{q_{\perp}^{(30.0)}} \cdot \frac{3}{2}, \quad a_{\parallel} = \frac{2}{\sqrt{3}q_{\parallel}^{(30.0)}} \cdot \frac{3}{2}, \quad (3.16)$$

$$(03.0) : a_{\perp} = \frac{2}{q_{\perp}^{(03.0)}} \cdot \frac{3}{2}, \quad a_{\parallel} = \frac{2}{\sqrt{3}q_{\parallel}^{(03.0)}} \cdot \frac{3}{2}, \quad (3.17)$$

$$(22.0) : a_{\perp} = \frac{4}{q_{\perp}^{(22.0)}}. \quad (3.18)$$

For detailed calculations and the origin of the factor $\frac{3}{2}$, see A.2. Again, lattice constants obtained from several reflections, the mean and standard deviation are calculated.

3.3.2 Results

The analysis of the data will not be structured into the 1st and 2nd batch, but into the analysis of (i) c -plane, (ii) r -plane and (iii) m - and a -plane samples. In the following, some general remarks on the fabricated samples will be made.

In Fig. 3.20, a detailed view into the growth rates of the samples of the 1st batch is given. First of all, for a fixed fluence (fixed lens position), increasing the pulse number decreases the growth rate. This is expected, because the coating of the laser entrance window increases during the process. By fixing a pulse number, an increase in growth rate is observed for a regime of decreasing fluence from 2 to 1 J cm^{-2} (Fig 3.20 bottom). This can be explained by the fact that the reduction of fluence is due to increasing laser spot size. When the fluence is still above the ablation threshold for the target material, an increasing ablation area results in an increasing growth rate. But at some point the fluence is too low to ablate the material and then the growth rate decreases, even though the ablation area increases. This can be observed at around 1.2 J cm^{-2} in Fig. 3.20,

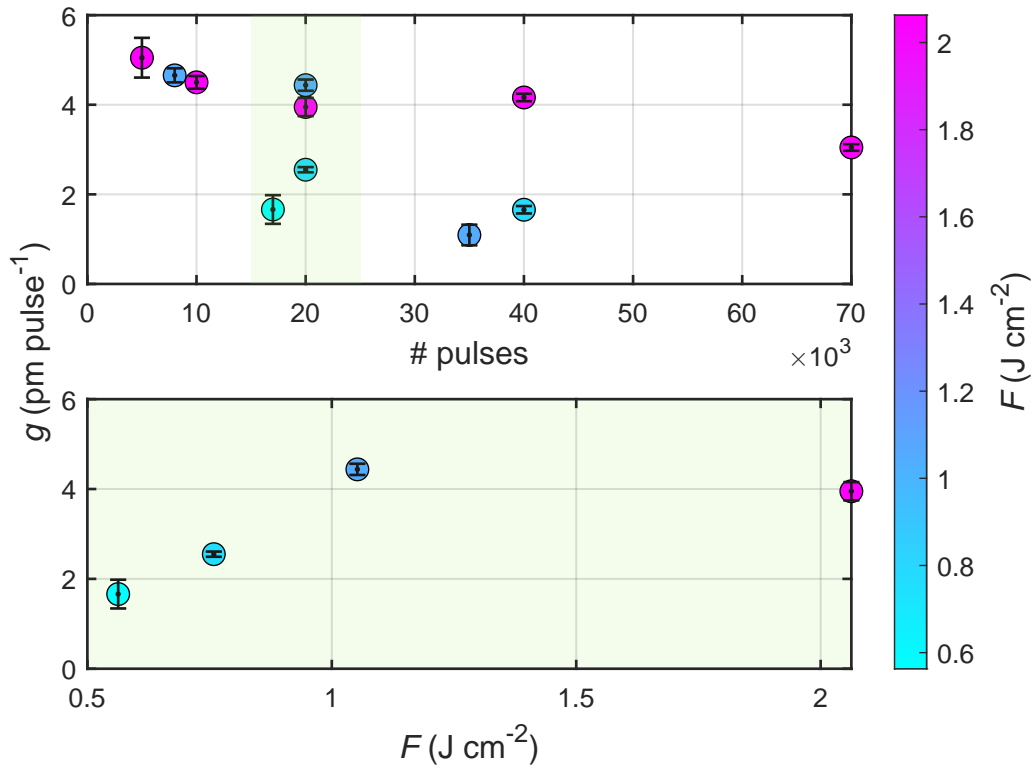


Figure 3.20: Growth rates of the samples from the 1st batch, depending on the pulse number (top) and depending on the laser fluence on the target for an approx. fixed pulse number (bottom). The data points are the mean of the four samples with another orientation each, that were obtained from every process. The errorbar displays the standard deviation.

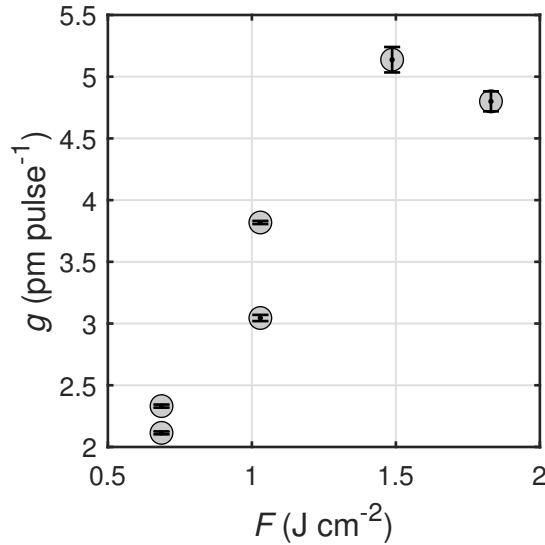


Figure 3.21: Growth rates of samples from the 2nd batch, depending on laser fluence on the target surface. The data points are the mean of thicknesses of the four orientations, similar to Fig. 3.20.

which is therefore an estimate for the ablation threshold. For the growth rates of the samples of the 2nd batch (Fig. 3.21), a similar conclusion can be drawn. Reducing the laser spot size below approx. 1.5 J cm^{-2} results in a decrease of growthrate from 5 to 2 pm pulse^{-1} . The ablation threshold can be localized between 1 J cm^{-2} and 1.5 J cm^{-2} .

In Fig. 3.22, the transmission spectra of selected m -plane oriented samples from the 1st batch are depicted. The fluence does not seem to have a significant influence, however, the thickness is decisive for the shape of the absorption edge. The onset of absorption E_τ is approx. 3.6 eV for all samples of different thickness and fluence. This is in accordance with the value obtained for the samples of the initial Cr_2O_3 batch (cf. 3.1 and Fig. 3.5b). But note that E_τ depends strongly on where the regime for linear fitting is set, so those values are only a rough estimate and should not be confused with the band gap.

c-plane: Laser Spot Size Variation

The o.o.p. strain calculated via Equ. (3.1) for all samples of the 1st batch is displayed in Fig. 3.23. Consider the c -plane oriented samples of the 1st batch, that had a fixed lens position yielding a fluence of approx. 2 J cm^{-2} , but varying thickness (brown squares in Fig. 3.23). A clear dependence of the o.o.p. strain can be observed: thinner samples yield higher strain. The layers become relaxed for thicknesses above approx. 170 nm . For low thicknesses, the strain approaches the predicted value for pseudomorphic growth of Cr_2O_3 on Al_2O_3 , which is 3.90% (cf. Tab. 1.3). The recorded RSMs of the (02.10) reflection can confirm whether this observation of o.o.p. strain is due to pseudomorphic growth. In Fig. 3.24, one can observe a shift of $q_{\parallel}^{(02.10)}$ to higher values for lower thicknesses. This corresponds to a decrease of the i.p. lattice constant, which is the expected behavior for pseudomorphic growth, because the i.p. a lattice constant of c -oriented Al_2O_3 is 0.2 \AA smaller than for Cr_2O_3 (cf. Tab. 1.1). The tensile o.o.p. strain observed

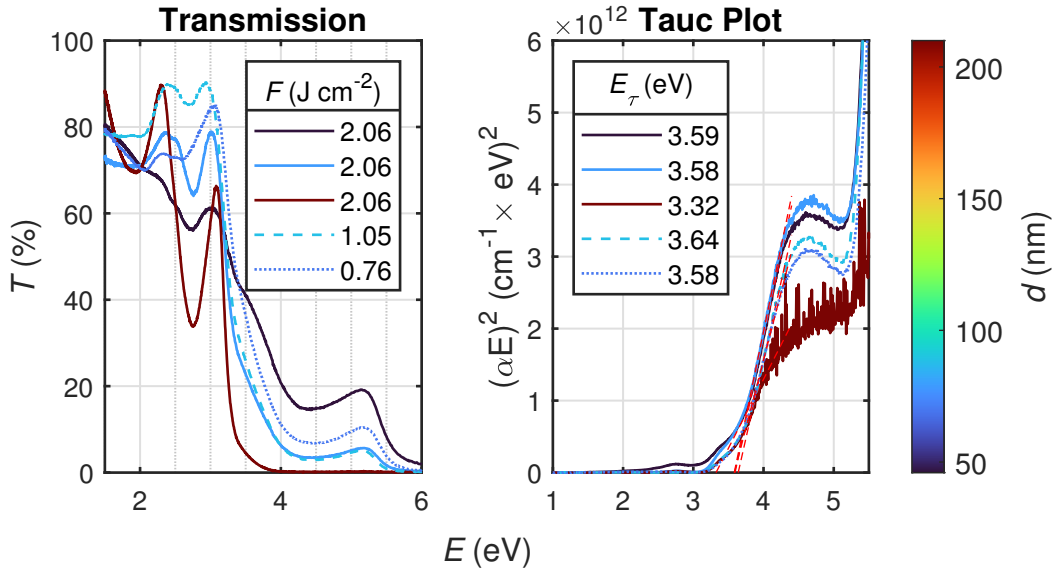


Figure 3.22: Transmission spectra (left) of selected m -plane oriented samples from the 1st batch. The samples differed in thickness and laser fluence on the target surface, achieved by varying lens positions. The TAUC-plot (right) of the mentioned samples, determined by assuming a direct band gap of Cr_2O_3 (cf. 3.1).

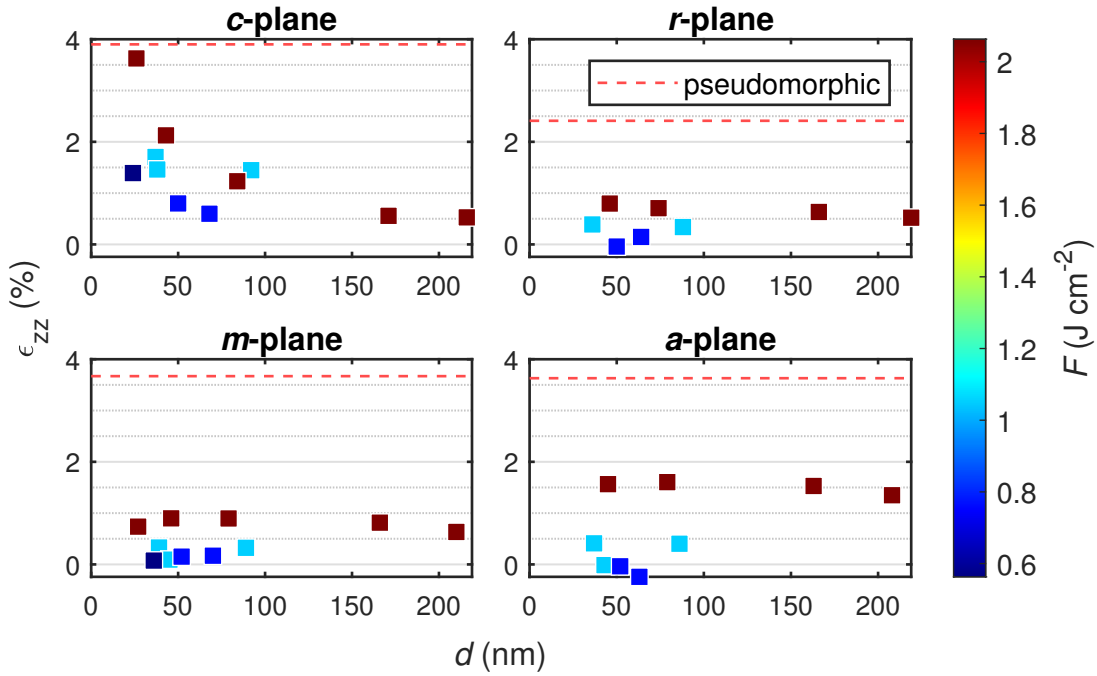


Figure 3.23: Out-of-plane strain calculated from $2\theta-\omega$ -patterns for all samples from the 1st batch, depending on thickness and laser fluence (false color).

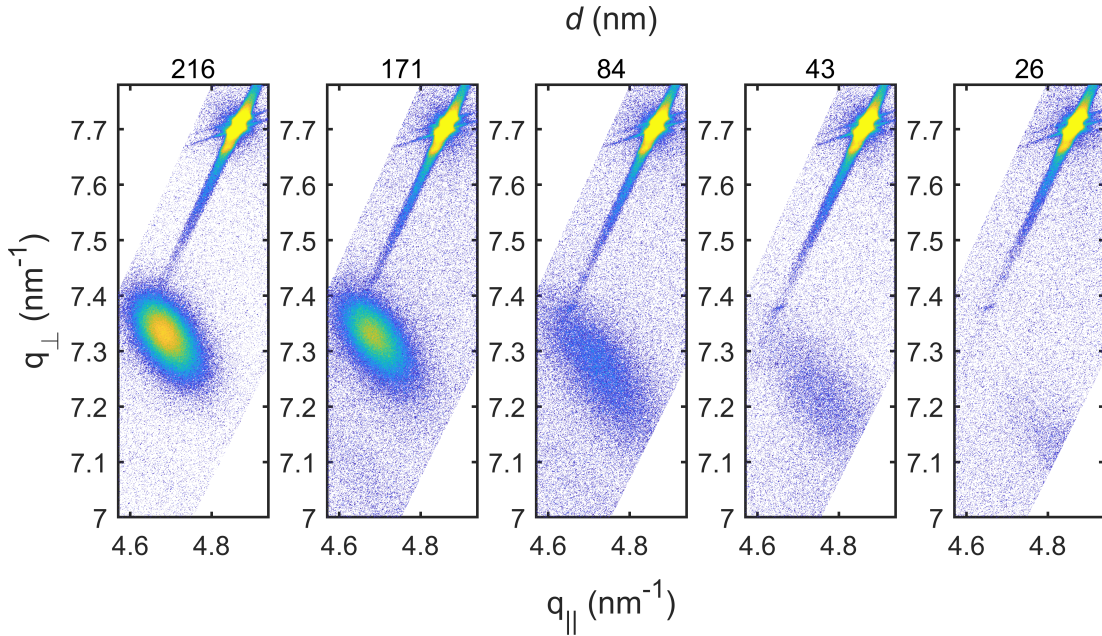


Figure 3.24: RSMs of the (02.10) reflection for several *c*-plane oriented samples of the 1st batch with varying thickness. The reflection in the upper right corner represents the (02.10) reflection of the sapphire substrate.

via 2θ - ω -scans can also be confirmed by the fact that the o.o.p. component $q_{\perp}^{(02.10)}$ is decreasing for thinner samples. The reduction of signal intensity is attributed to the thickness, but could also be a result of decreasing crystal quality (cf. Fig. 3.25). When looking into the remaining samples that were fabricated with larger laser spot sizes but similar thickness (bluish squares in Fig. 3.23), it becomes clear that the o.o.p. strain is also slightly reduced for lower fluences. But note that this effect is less dominant when compared to the influence of thickness.

In Fig. 3.25, the ω -FWHM is depicted depending on the film thickness and laser fluence for the 1st batch. As before, consider the samples with smallest laser spot size (largest fluence) first: increasing the thickness is clearly correlated to a decreasing ω -FWHM. Therefore, thicker samples yield both less strained and more crystalline films. Note that there is an outlier to this behavior for the sample with a thickness of approx. 30 nm. When considering the ω -pattern (Fig. B.1a), it becomes clear that the non-VOIGT shape makes the determination of Full Width at Half Maximum (FWHM) difficult. Therefore, not too much attention should be paid to this data point. When considering the samples fabricated with lower fluences (bluish squares in Fig. 3.25), a much more dominant influence of laser spot size on the crystallinity can be observed. This can be summarized by stating that the thickness of samples is the dominant influence on the o.o.p. strain, because the thickest samples yielded less strain than the thinner samples with lowest fluence (Fig. 3.23). However, for the ω -FWHM, it is the other way around, namely that even the thinnest samples (which exhibit better quality than thinner samples of same lens position) have a much higher ω -FWHM when compared to thinner samples fabricated with less fluence. This can be seen in Fig. 3.26, where the ω -FWHM is visualized depending on the o.o.p. strain of the corresponding sample: A linear behavior (correlation) is observed for each set fluence; but there are

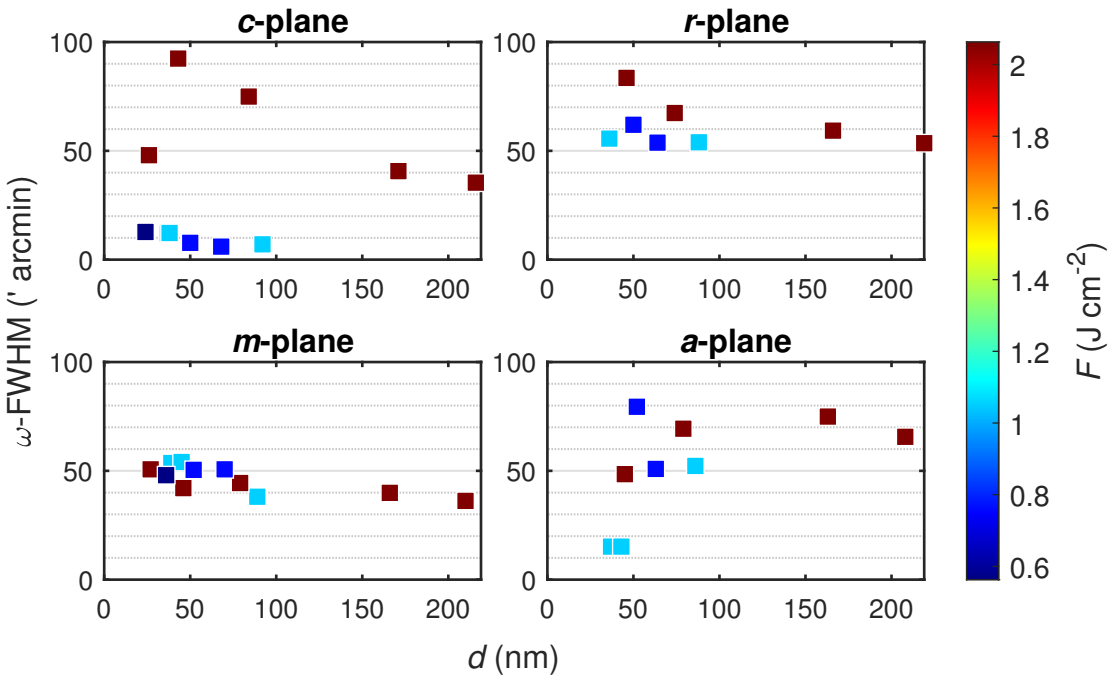


Figure 3.25: ω -FWHM for all samples from the 1st batch, depending on thickness and laser fluence (false color). The corresponding diffractograms are depicted in Fig. B.3.

two different regimes in total, with the high-fluence regime generally showing higher ω -FWHM.

c-plane: Pulse Energy Variation

The o.o.p. strain for the *c*-plane oriented samples fabricated with various laser pulse energies, but constant laser spot size, are depicted in Fig. 3.27. Note that there is still a distribution of thickness from 100 to 200 nm, even though the pulse number was adapted to the corresponding laser pulse energy. The strain is overall smaller ($< 2\%$) than for the 1st batch, because the 2nd batch contained samples with thickness $t > 100$ nm which yields smaller strains as seen before. No systematic dependence on the laser fluence is observed, which may be explained by the still remaining thickness distribution which overlaps the fluence variation. This effect could be strong enough to overshadow the impact of laser pulse energy, as it was shown in the previous experiment that the thickness is the dominant factor for the o.o.p. strain. For example, note the sample fabricated with $F = 1.5 \text{ J cm}^{-2}$ (green square in Fig. 3.27), which exhibits the lowest strain, even though having higher fluence value than other samples. This can be explained by the fact that with $t = 200$ nm, it is the thickest sample of the batch.

In Fig. 3.28, the ω -FWHM is depicted depending on the laser fluence and film thickness for the 2nd batch. The previously observed relation is confirmed: increasing fluences result in higher ω -FWHMs. Namely, reducing the fluence by a factor of 2 results in a crystal quality improvement by one order of magnitude. Note that for a fluence of approx. 1 J cm^{-2} , two samples A and B with same thickness of 150 nm exhibit very different ω -FWHM of $\Delta\omega_A = 8'$ and $\Delta\omega_B = 49'$. The ω -patterns are depicted in Fig. B.1b. Note that both diffractograms have VOIGT shape, so the discrepancy may not be attributed to the determination of the FWHM. On the contrary, note that

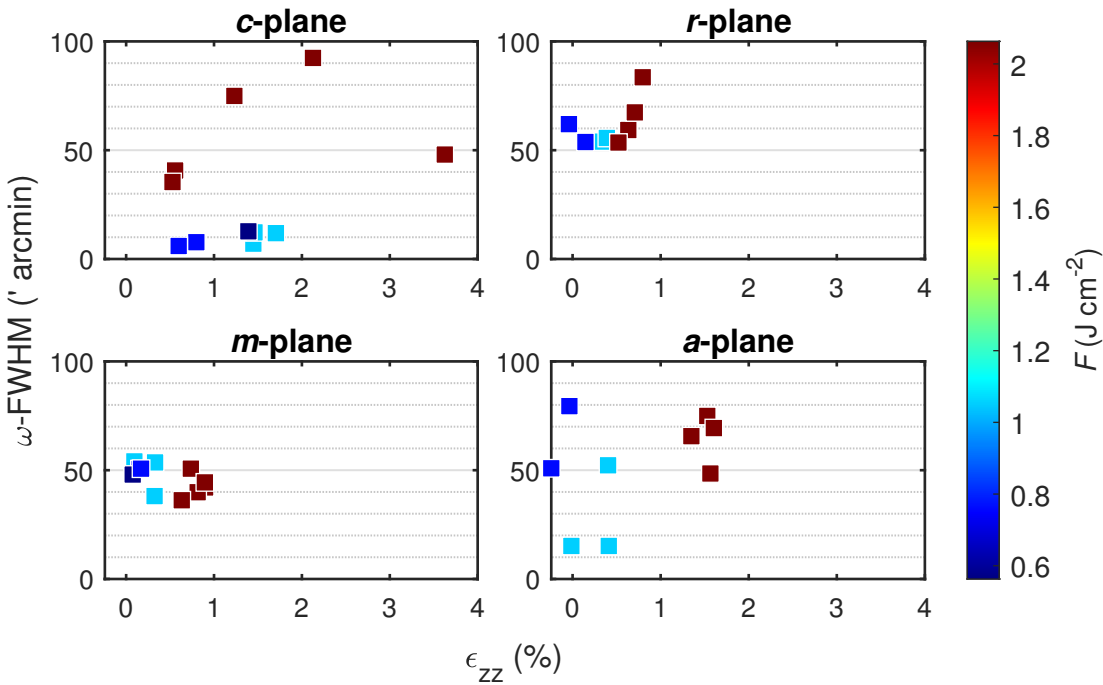


Figure 3.26: Correlation between strain and ω -FWHM for all samples from the 1st batch, depending on thickness and laser fluence (false color).

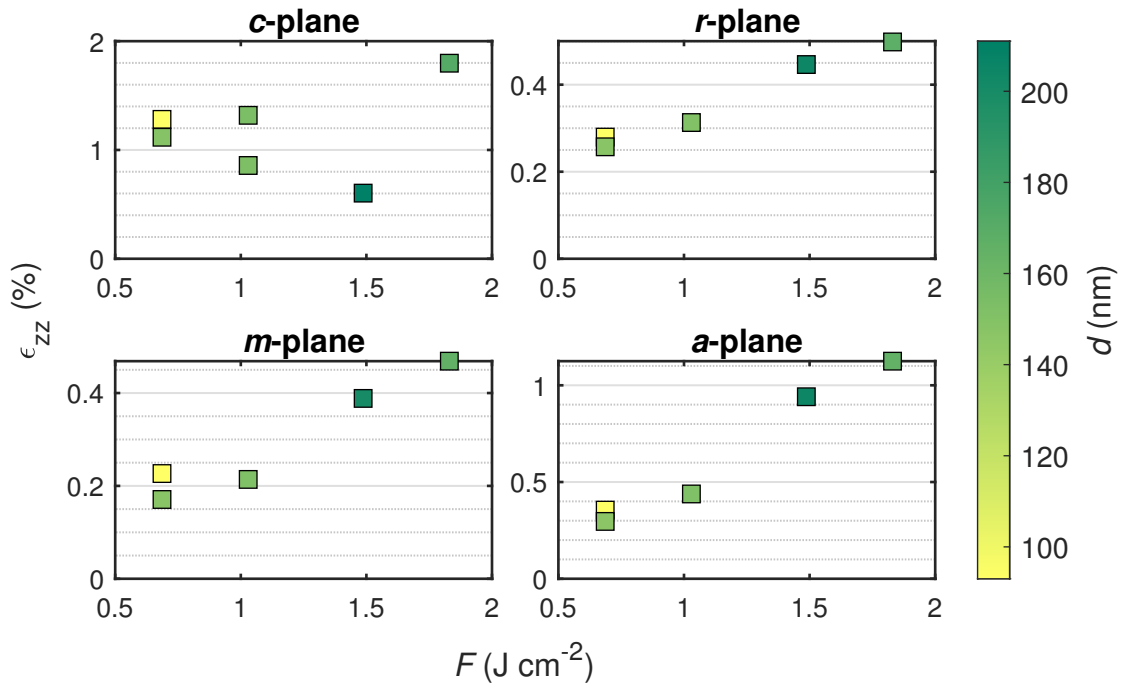


Figure 3.27: Out-of-plane strain calculated from 2θ - ω -patterns for all samples from the 2nd batch, depending on laser fluence and thickness (false color).

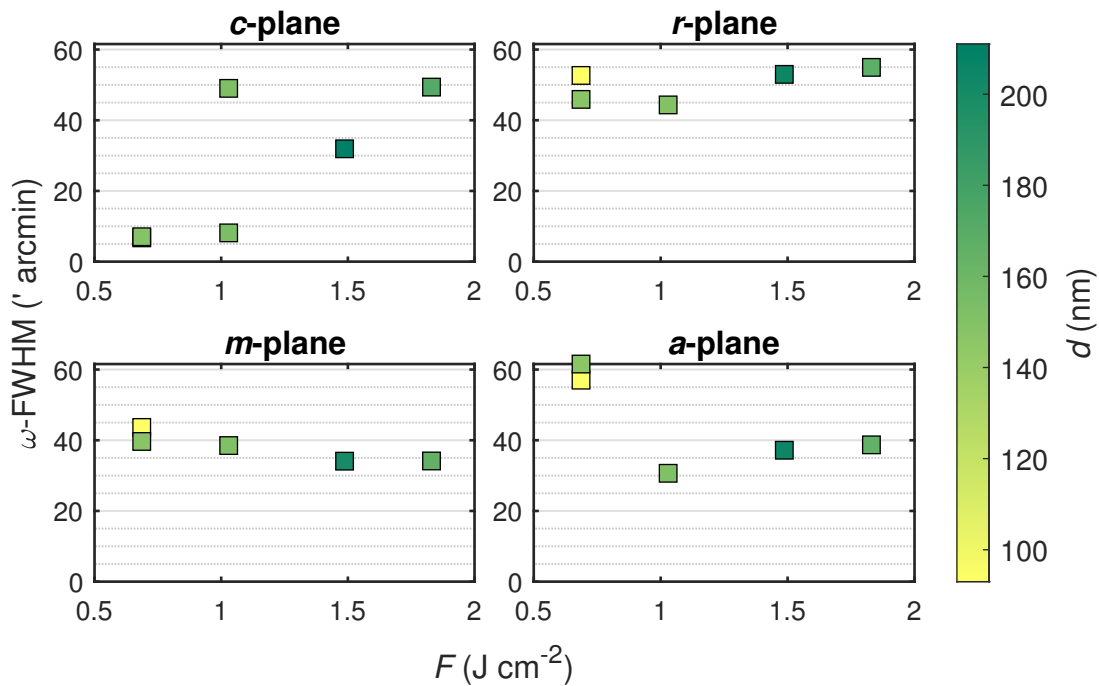


Figure 3.28: ω -FWHM for all samples from the 2nd batch, depending on laser fluence and thickness (false color). The corresponding diffractograms are depicted in Fig. B.4.

for the whole process B, a determination of FWHM was possible only for the *c*-plane samples⁽¹²⁾. In Fig. B.2, the ω -patterns of samples of all orientations from this process are depicted. The non-VOIGT shape for the orientations other than *c*-plane as well as the unexpectedly high ω -FWHM for *c*-plane sample indicate that the process yielded samples with poor crystal quality. The origin of this observation is not entirely clear, but for some samples of this batch, the stepper motor causing the substrate rotation stopped during deposition, resulting in non-uniform deposition. Whether this was the case for process B is not sure, but since both A and B were conducted with the same process parameters⁽¹³⁾, something irregular must have been occurred.

r-plane: Laser Spot Size Variation

In Fig. 3.23, the o.o.p. strain for the *r*-plane samples fabricated with varying laser spot size is shown. The overall strain is with less than 1 % lower when compared to the *c*-plane samples, exhibiting values up to 4 % for thin samples. In particular, the predicted value for o.o.p. strain during pseudomorphic growth of Cr_2O_3 on Al_2O_3 of 2.41 % is not reached (cf. Tab. 1.3). As can be seen in a detailed view (Fig. B.5), the strain depends on the thickness: it decreases from 0.8 % to 0.5 % for an increment of thickness from 50 nm to 200 nm. This is in accordance to the behavior observed for the *c*-plane samples, albeit less pronounced. Furthermore, for a fixed thickness, decreasing the fluence also results in less strained thin films, which is similar to the behavior of the *c*-plane samples. The ω -FWHM obtained from the (02.4) reflection is depicted in Fig. 3.25. Similar to the *c*-

⁽¹²⁾ This is why in Fig. 3.28, only the upper left *c*-plane tile has two data points at $F \approx 1 \text{ J cm}^{-2}$.

⁽¹³⁾ The pulse number was varying, however, the growth rates $g_A = 3 \text{ pm pulse}^{-1}$ and $g_B = 3.75 \text{ pm pulse}^{-1}$ were quite similar.

plane samples – but less pronounced–, increasing the thickness results in less mosaicity, which is also achieved by reducing the fluence. Note that the overall ω -FWHM is between 50' and 90' which differs for the *c*-plane samples, where a lower fluence yielded samples with $\Delta\omega < 10'$ (cf. Fig. 3.25). Therefore, increasing the thickness and reducing the fluence by varying laser spot position may increase the crystal quality, but not to an amount comparable to *c*-plane oriented thin films.

r-plane: Pulse Energy Variation

In Fig. 3.27, the o.o.p. strain is depicted for varying laser pulse energies (2nd batch). Independent of thickness, the fluence determines the strain of the thin films. The overall strain is below 0.4 %, and thereby comparable to the samples obtained from processes in the 1st batch with larger laser spot sizes. A detailed view on the strain for those samples is given in Fig. ?? which is based on the evaluation of RSMs that were performed as described in 3.3.1. The o.o.p. strain was calculated from both asymmetric (green triangle) and symmetric (yellow squares) reflections. The latter is equivalent to the calculation from the peak position in $2\theta-\omega$ diffraction patterns. It can be observed that the increasing tensile o.o.p. strain comes along with an increasing i.p. compressive strain, ranging from -0.2 % to -0.8 %. Therefore, the o.o.p. strain may be attributed to a partial pseudomorphic growth mode, because the Al_2O_3 lattice constants are smaller than the ones for Cr_2O_3 . The compressive strain is then due to an aligning of in-plane lattice constants. Note that the values for o.o.p. strain obtained from $2\theta-\omega$ -scans (cf. Fig. 3.27) are only partially confirmed: the strain measured from the symmetric RSM is approx. 0.2 percentage points below the value obtained from $2\theta-\omega$ -scans. The origin of this discrepancy may lay in the correction that was applied the RSMs. However, the correction of the substrate peak position in 2D reciprocal space corresponds to a shift of the whole 1D $2\theta-\omega$ pattern to match the substrate peak. The latter was done for the evaluation of $2\theta-\omega$ -scans on which Fig. 3.27 is based. But the correction of thin film tilt which is done for RSMs was not done for the $2\theta-\omega$ -scans⁽¹⁴⁾ (because the information on thin film tilt is not provided by a $2\theta-\omega$ -pattern). But even though this is a significant difference in evaluation between $2\theta-\omega$ -patterns and RSMs, the discrepancy between both methods is still present even for small thin film tilts below 10'. So further analysis has to be done for the applied evaluation methods. But in general it has to be noted that the precision of the o.o.p. strain obtained from RSMs depends on (i) the peak position of the reflection, (ii) the peak position of the corresponding substrate peak (for substrate correction) and (iii) the peak position of the asymmetric peaks (for shear correction, not done for *r*-plane). Those positions were not obtained by fitting a 2D VOIGT profile to the RSMs, but by reading the peak position “by hand”. This may result in an undefined error.

Another observation is that the o.o.p. strain obtained from symmetric (yellow squares) and asymmetric reflections (green triangles) aligns for the two samples fabricated with higher fluences only (cf. Fig. 3.29). The discrepancy observed for the lower fluences is physically implausible and is probably due to an error in evaluation. This is supported by the fact that for those two data points, the strain obtained from asymmetric re-

⁽¹⁴⁾ The ω -optimization prior to a $2\theta-\omega$ -scan is for correcting a tilt of the whole sample, because 2θ is fixed to the value expected for the (02.4) reflection of Al_2O_3 . This does not account for a possible thin film tilt with respect to the substrate.

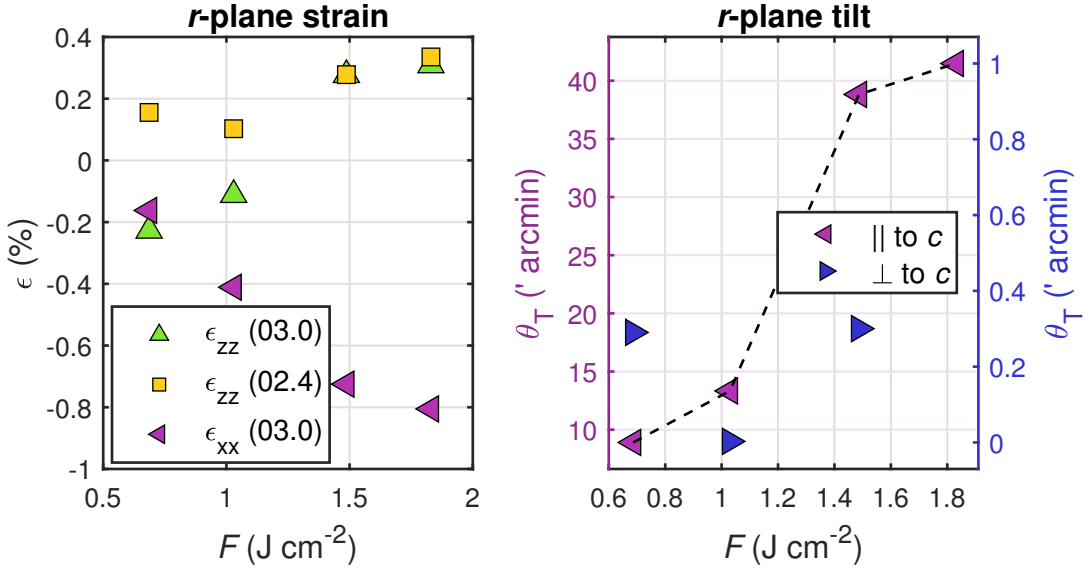


Figure 3.29: In-plane and out-of-plane strain for the *r*-plane samples from the 2nd batch, calculated from the peak positions of the RSMs described in 3.3.1.

flections is almost exactly mirroring the value obtained from the symmetric reflections. This also confirms the previously stated hypothesis that the evaluation of either RSM or 2ϑ - ω -pattern exhibits a systematic error.

As predicted by Grundmann and Lorenz (2020) [1], partially relaxed *r*-plane thin films with certain values for the elastic tensor should exhibit a tilt of the thin film with respect to the substrate. This tilt is indeed observed along the *x*-axis for all values of fluence, ranging from approx. $10'$ to $40'$ (purple triangles in Fig. 3.29). A corresponding tilt along the *y*-axis is not observed: there, the tilt angles are two orders of magnitude lower and below $0.4'$. This is in agreement with elasticity theory which predicts a tilt only along the *x*-axis, because the prismatic slip systems responsible for relaxation along the *y*-axis yield tilt components of the BURGER's vector that cancel out on average (cf. 1.3.2). But note that the thin film tilt increases for higher fluences, which also results in a higher o.o.p. strain. This observation is somehow curious, because the thin film tilt is a result of *relaxation*, whereas strain is a result of partial *pseudomorphic* growth. So according to strain, higher fluences result in less relaxed layers – according to tilt, higher fluences result in more relaxed layers. This result indicates that an interplay of both processes is present and that for growth modes that exhibit no complete pseudomorphic behavior, more sophisticated models for the relaxation mechanism must be applied.

The ω -FWHM of the *r*-plane samples of the 2nd batch is approx. $50'$ and has no significant dependence on both fluence or thickness (Fig. 3.28). This confirms the previously obtained result for the samples fabricated with varying laser spot sizes.

Appendices

Appendix A

Calculations

In the following, Equ. 2.7 is applied:

$$d_{hkl} = \left(\frac{4}{3} \frac{h^2 + k^2 + hk}{a^2} + \frac{l^2}{c^2} \right)^{-1/2}.$$

A.1 *m*-plane lattice constants

The reflection $(30.\pm 6)$ is a superposition of out-of-plane (30.0) and in-plane $(00.\pm 6)$. The inverse lattice plane distances are

$$q_{\perp}^{(30.\pm 6)} = d_{(30.0)}^{-1} = \sqrt{\frac{4}{3} \frac{3^2}{a^2}} = \sqrt{12}/a, \quad (\text{A.1})$$

$$q_{\parallel}^{(30.\pm 6)} = d_{(00.\pm 6)}^{-1} = \sqrt{\frac{(\pm 6)^2}{c^2}} = 6/c. \quad (\text{A.2})$$

In the y -axis azimuth, $(4\bar{2}.0)$ is a superposition of out-of-plane (30.0) and in-plane $(1\bar{2}.0)$. Note that $(1\bar{2}.0)$ has a -plane character. The inverse lattice plane distances are

$$q_{\perp}^{(4\bar{2}.0)} = d_{(30.0)}^{-1} = \sqrt{12}/a, \quad (\text{A.3})$$

$$q_{\parallel}^{(4\bar{2}.0)} = d_{(1\bar{2}.0)}^{-1} = \sqrt{\frac{4}{3} \frac{1^2 + 2^2 - 2}{a^2}} = 2/a. \quad (\text{A.4})$$

Also in this azimuth, (22.0) is a superposition of out-of-plane (30.0) and in-plane $(\bar{1}2.0)$. The inverse lattice plane distances are

$$q_{\perp}^{(22.0)} = d_{(30.0)}^{-1} = \sqrt{12}/a, \quad (\text{A.5})$$

$$q_{\parallel}^{(22.0)} = d_{(\bar{1}2.0)}^{-1} = \sqrt{\frac{4}{3} \frac{1^2 + 2^2 - 2}{a^2}} = 2/a. \quad (\text{A.6})$$

A.2 *a*-plane lattice constants

The reflection $(22.\pm 6)$ is a superposition of out-of-plane (22.0) and in-plane $(00.\pm 6)$. The inverse lattice plane distances are

$$q_{\perp}^{(22.\pm 6)} = d_{(22.0)}^{-1} = \sqrt{\frac{4}{3} \frac{2^2 + 2^2 + 4}{a^2}} = 4/a, \quad (\text{A.7})$$

$$q_{\parallel}^{(22.\pm 6)} = d_{(00.\pm 6)}^{-1} = 6/c. \quad (\text{A.8})$$

In the y -axis azimuth, (30.0) cannot be represented as a superposition of in-plane and out-of-plane scattering vectors. This is due to the symmetry of the hexagonal lattice. But it is possible to represent it as a superposition of out-of-plane (11.0) and in-plane $(1\bar{1}.0)$, multiplied with a factor of 1.5 each. This leads to the calculation of inverse lattice planes via

$$q_{\perp}^{(30.0)} = \frac{3}{2} \cdot d_{1\bar{1}.0}^{-1} = \frac{3}{2} \sqrt{\frac{4}{3} \frac{1^2 + 1^2 - 1}{a^2}} = \frac{3}{2} \cdot \frac{2}{\sqrt{3}}/a = \sqrt{3}/a, \quad (\text{A.9})$$

$$q_{\parallel}^{(30.0)} = \frac{3}{2} \cdot d_{11.0}^{-1} = \frac{3}{2} \sqrt{\frac{4}{3} \frac{1^2 + 1^2 + 1}{a^2}} = \frac{3}{2} \cdot 2/a = 3/a. \quad (\text{A.10})$$

The same holds for the (03.0) reflection: it is a superposition of $(\bar{1}1.0)$ and (11.0) , multiplied by a factor of 1.5 and one obtains:

$$q_{\perp}^{(03.0)} = \frac{3}{2} \cdot d_{\bar{1}1.0}^{-1} = \sqrt{3}/a, \quad (\text{A.11})$$

$$q_{\parallel}^{(03.0)} = \frac{3}{2} \cdot d_{11.0}^{-1} = 3/a. \quad (\text{A.12})$$

Appendix B

Figures

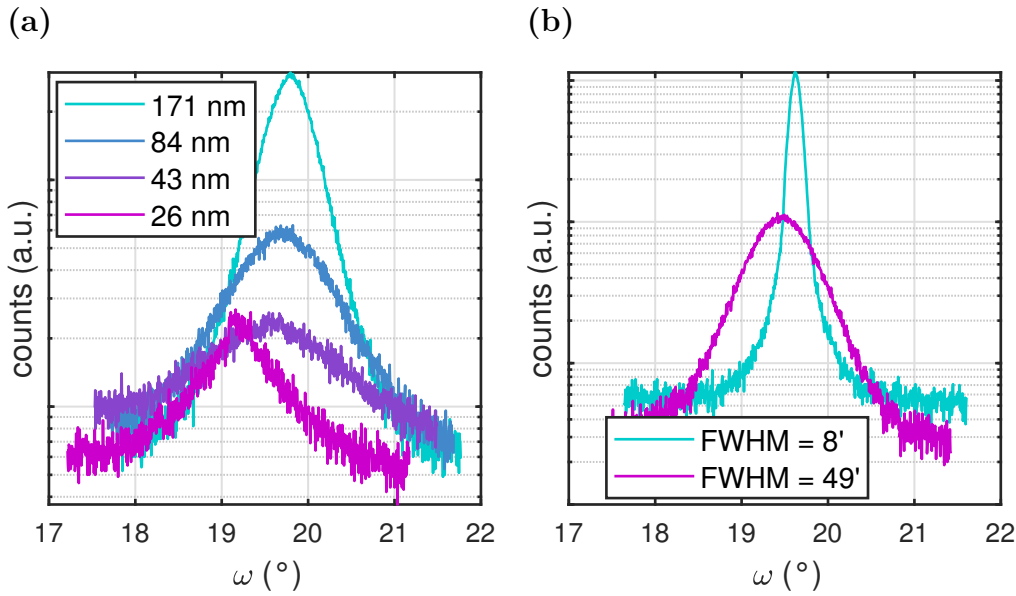


Figure B.1: (a) ω -patterns for c -plane oriented samples of the 1st batch in 3.3, fabricated with smallest laser spot size. (b) ω -patterns for two c -plane oriented samples from the 2nd batch in 3.3, that were fabricated with same fluence and had the same thickness of approx. 150 nm, but very different ω -FWHM.

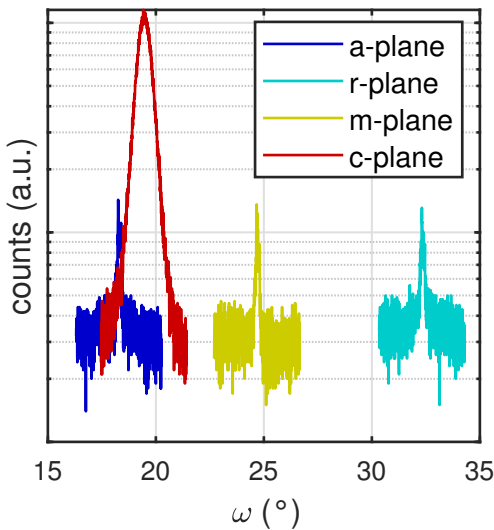


Figure B.2: ω -patterns for the samples of the process that yielded the c -plane sample with higher FWHM in Fig. B.1b. The patterns correspond to c - (red), r (cyan), m (yellow) and a -plane (blue).

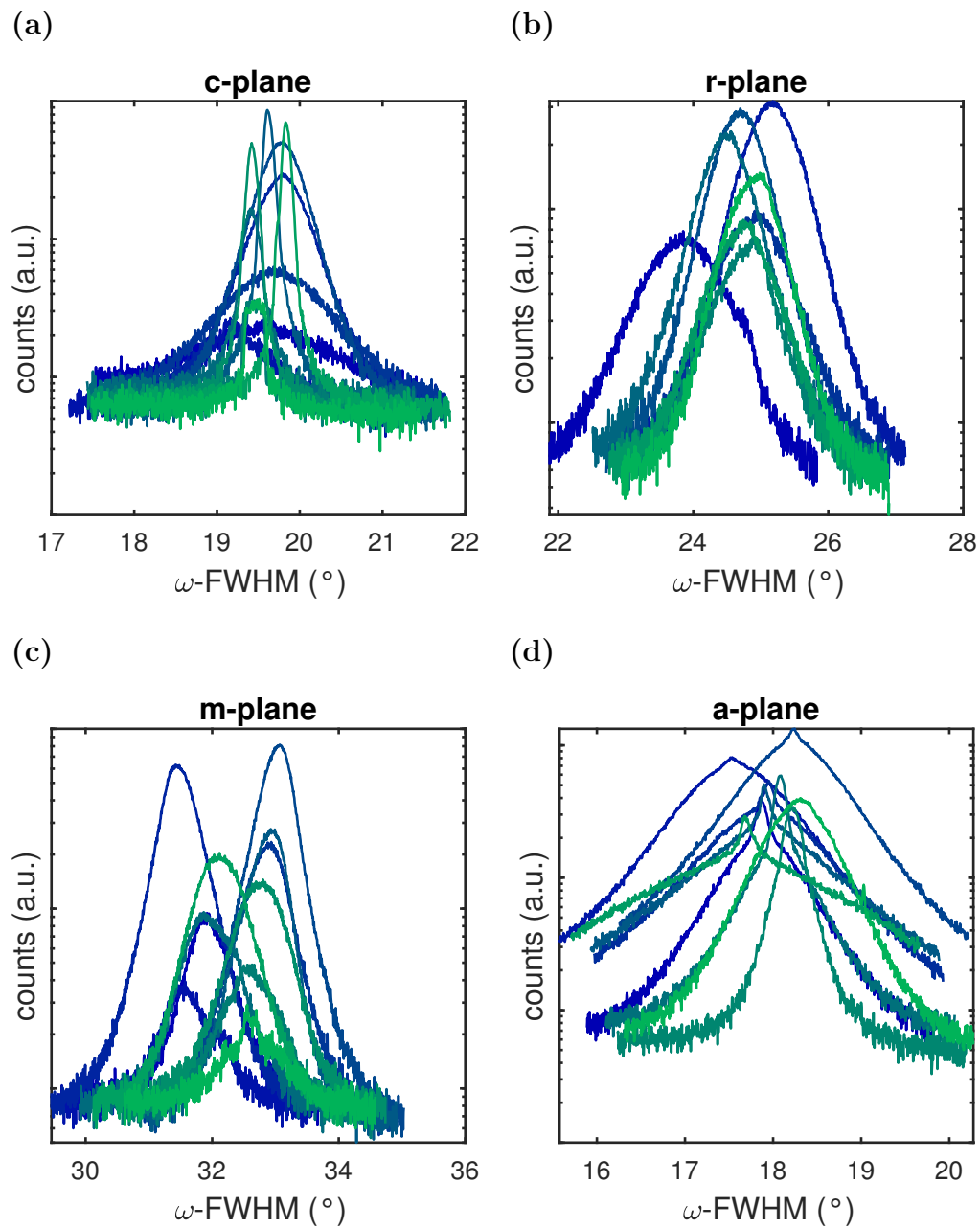


Figure B.3: Diffractogramms from ω -patterns for varying laser focus in 3.3.

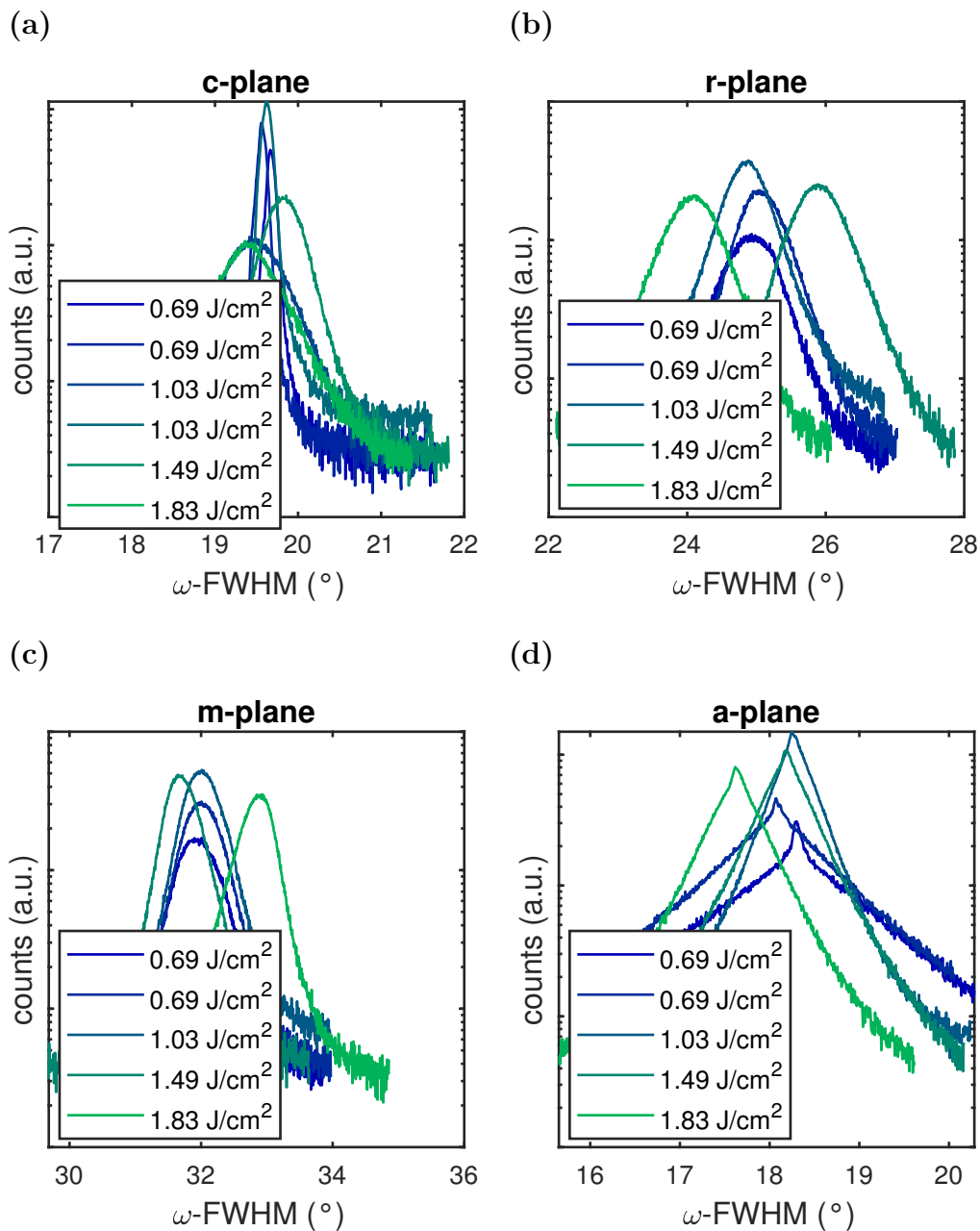


Figure B.4: Diffractogramms from ω -patterns for varying laser pulse energy in 3.3.

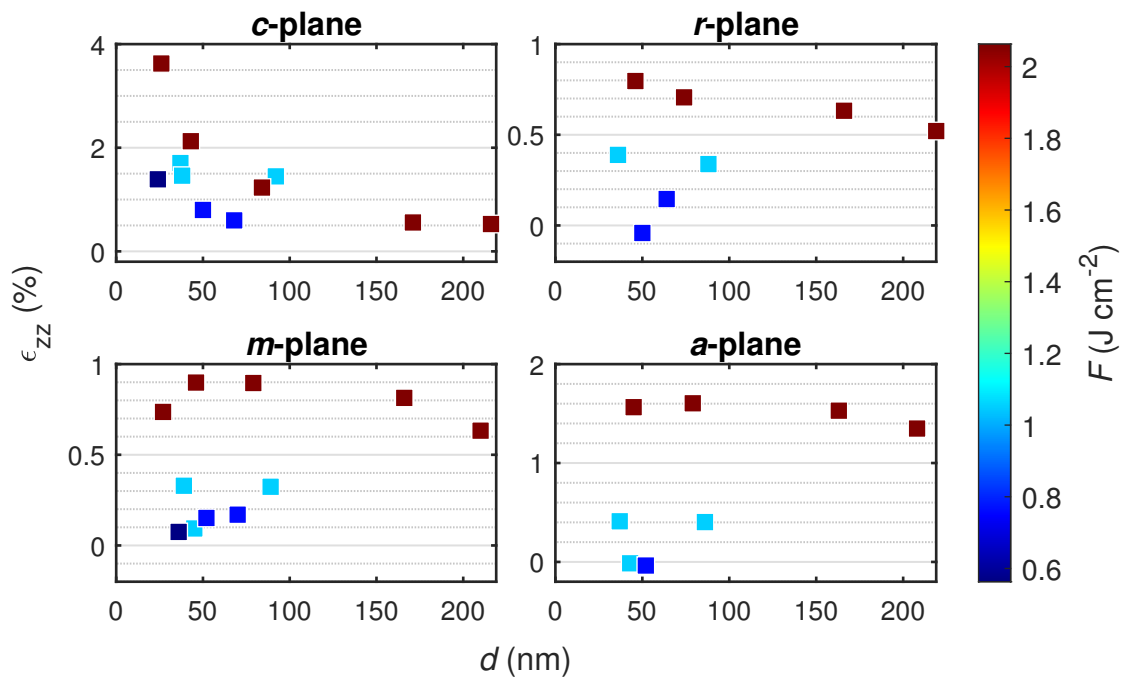


Figure B.5: Detailed view (cf. Fig. 3.23) of the o.o.p. strain for the samples of the 1st batch in 3.3.

Bibliography

- [1] M. Grundmann and M. Lorenz. “Anisotropic strain relaxation through prismatic and basal slip in α -(Al, Ga)₂O₃ on R-plane Al₂O₃”. In: *APL Materials* 8.2 (2020), p. 021108. ISSN: 2166-532X. DOI: [10.1063/1.5144744](https://doi.org/10.1063/1.5144744).